Supplementary Information

Hierarchically heterogeneous interface structuring strategy for microenvironment-regulating and self-decontaminating biodegradable meta-membranes

Author Information

Affiliations

Shao-Zhen Wang[1], Xinjian He[1,6]*, Xing-Hua Wei[4], Guiying Zhu[2], Jia-Lian Gao[1], Zhuang Huang[2], Yue Zhao[3], Xiao-Peng Li[3], Jiefeng Gao[5] & Huan Xu[2,6]*

[1]School of Safety Engineering, China University of Mining and Technology, Xuzhou 221116, China.

[2]School of Materials Science and Physics, China University of Mining and Technology, Xuzhou 221116, China.

[3]State Key Laboratory of Chemistry for NBC Hazards Protection, Beijing 102205, China

[4]Hangzhou WOQU Technology Co., Ltd., Hangzhou 310052, China

[5]School of Chemistry and Chemical Engineering, Yangzhou University, Yangzhou 272100, China

[6]Jiangsu Engineering Research Center of Dust Control and Occupational Protection, Xuzhou 221008, China.

Contributions

H.X. and X.J.H. conceived the idea and designed the experiments. S.-Z.W. and G.Y.Z. performed the experiments. X.H.W., J.-L.G., Z.H., and Y.Z. contributed to materials characterizations. X.-P.L. and G.J.F. joined the discussion of the data and gave helpful suggestions. S.-Z.W. and H.X. wrote the manuscript. All authors participated in drafting the paper, and gave approval to the final version of the manuscript.

Corresponding authors

Correspondence to: xinjian.he@cumt.edu.cn, hihuan@cumt.edu.cn

Content

54

List of Abbreviations

Abbreviation	**Definition**
HHIS	Hierarchically Heterogeneous Interface Structuring
MRSD-PLA	Microenvironment-Regulating and Self-Decontaminating Poly(lactic acid) Meta-Membranes
PLA	Poly(lactic acid)
ZIF-8	Zeolitic Imidazolate Framework-8
F-TiO_2	Fluorinated Titanium Dioxide
MOF	Metal-Organic Framework
PM	Particulate Matter
$PM_{0.3}$	Particulate Matter with a Diameter of 0.3 Micrometers or Smaller
$PM_{2.5}$	Particulate Matter with a Diameter of 2.5 Micrometers or Smaller
QF	Quality Factor
WVTR	Water Vapor Transmission Rate
RH	Relative Humidity
BET	Brunauer–Emmett–Teller
PSD	Pore Size Distribution
NLDFT	Non-Local Density Functional Theory
XRD	X-Ray Diffraction
FTIR	Fourier-Transform Infrared Spectroscopy
SEM	Scanning Electron Microscopy
TGA	Thermogravimetric Analysis
ROS	Reactive Oxygen Species
DMF	N,N-Dimethylformamide
DCM	Dichloromethane
TTIP	Titanium (IV) Isopropoxide
IPA	Isopropyl Alcohol
EtOH	Ethanol

PFOTES	1H,1H,2H,2H-Perfluorooctyltriethoxysilane

Supplementary Notes

Note S1. Characterization

The morphological and compositional characteristics of the electroactive ZIF-8 nanocrystals, hydrophobic F-TiO_2 nanoblocks and MRSD-PLA were investigated using a Hitachi SU8220 scanning electron microscope (SEM) equipped with energy-dispersive X-ray spectroscopy (EDS). Quantitative analysis of fiber diameter distribution was performed based on SEM micrographs using ImageJ image processing software. The surface potential and dielectric properties of the fiber membranes were systematically characterized using a JH-TEST non-contact electrostatic voltmeter and a WK-6500B precision dielectric analyzer, respectively. Crystallographic structures were analyzed by X-ray diffraction (XRD) (2θ = 5-60°, $5°\cdot min^{-1}$) using a Bruker D8 Advance diffractometer (Germany), while chemical functional groups were identified through Fourier-transform infrared spectroscopy (FTIR) measurements conducted on a PerkinElmer Spectrum 3 spectrometer (USA). Nitrogen adsorption-desorption measurements at 77 K were performed using a Micro VacPrep061 machine. The pore size distribution of MRSD-PLA was characterized using a capillary flow porometer (CFP-1100AI, Porous Materials, USA). The water contact angle (WCA) of MRSD-PLA was determined using a contact angle goniometer (Kino SL200B, USA). The mechanical property of MRSD-PLA was tested using a universal test instrument (GT-7010, China). The electrostatic potential (ESP)-mapped electron densities of PLA chains were characterized by Gaussian. The thermal stability was evaluated using a TGA/DSC 2 type thermal analyzer (TGA) under a nitrogen atmosphere with a heating rate of 10 °C/min from ambient temperature to 800 °C.

Mechanical properties testing

In this study, a GT-7010 mechanical testing machine (Gaotai Testing Machine Co., Ltd.) was used to determine the mechanical properties of the samples. The samples were cut into rectangular strips measuring 5 cm × 1 cm, and five independent repeat measurements were performed on each discrete sample. The mean value and standard deviation of the mechanical parameters of the samples were calculated to comprehensively evaluate their mechanical properties.

Water contact angle and self-cleaning performance test

The surface wettability of the fiber membrane samples was quantitatively analyzed by using a contact angle measuring instrument. During the testing process, deionized water droplets (3 μL) were vertically added to the surface of the sample. The static contact angle value was automatically collected and calculated using the software provided with the instrument. Each group of samples was measured in parallel five times, and the average value was taken as the final result. To systematically evaluate the hydrophobic properties of the nanofiber membrane surface, common liquids with different surface tensions (including deionized water, carbonated beverages, coffee, milk and tea solutions) were selected for wettability tests. 50 μL of the test liquid was vertically dropped onto the surface of the sample placed horizontally, and the process of droplet morphology change was recorded using a high-speed camera[1].

To explore the self-cleaning performance of the samples, in this study, standard quartz sand was evenly scattered on the surface of the samples as a simulated contaminator. The surface of the samples was cleaned with deionized water for 30 seconds, and the residual contaminants on the surface were finally observed[2].

Breathability and moisture permeability test

Gas permeation properties were evaluated via the differential pressure method. Membrane samples (20 cm^2 effective area) were sealed between two chambers: the upstream chamber was charged with high-purity test gases at constant pressure (100 kPa), while the downstream chamber was maintained under vacuum. Steady-state gas flux was quantified using a soap-film flowmeter and calculated according to Fick's diffusion law[3]:

$$\boldsymbol{P} = \frac{\boldsymbol{J} \times \boldsymbol{d}}{\boldsymbol{\Delta P}} \qquad (\boldsymbol{S1})$$

Where P is the gas permeability coefficient (Pa), d is the membrane thickness (μm), and ΔP is the transmembrane pressure difference (Pa).

Moisture permeation testing employed the standard cup method under controlled conditions (40 °C, 90 ± 2% RH). The cited threshold of >2000 $g \cdot m^{-2} \cdot d^{-1}$ is based on industry standards for protective textiles (ISO 15496, ASTM F1868), which also specify comparable testing environments to ensure consistent performance evaluation across materials. The membranes were sealed over a cup containing desiccant to establish a humidity gradient. Mass increment of the cup was periodically recorded using an electronic balance. Water vapor transmission rate (WVTR) was derived from the mass change per unit time during the steady-state phase normalized to the effective area of the membrane[4]:

$$\boldsymbol{WVTR} = (\boldsymbol{\Delta m}/\boldsymbol{\Delta t}) \times (\mathbf{24}/\mathbf{A}) \qquad (\boldsymbol{S2})$$

Where Δm is the mass increment (g), Δt is the test time (h), and A is the membrane moisture permeability area (m^2). Each set of samples was tested three times, and the results were expressed as the mean and standard deviation. Data was collected at 1-hour intervals to ensure steady-state accuracy.

Air purification performance evaluation

To systematically evaluate the interception performance of fiber membrane filters against aerosol particles, the study employed a homemade air filtration evaluation system to conduct indoor pm filtration performance tests. During the experiment, a Model 8026 NaCl aerosol generator produced by TSI Incorporated in the USA was utilized to generate aerosol particles with a particle size distribution ranging from 0 to 10 μm. A precision gas flow pump was employed to precisely control the airflow rates at four distinct gradients: 10, 32, 65, and 85 L·min^{-1}. Concurrently, a high-precision differential pressure gauge was used to monitor the pressure difference across the filter in real-time. For the detection of aerosol concentration, a TSI Model 3910 nanoparticle analyzer was adopted. This sophisticated instrument is capable of accurately measuring the concentration changes of aerosols before and after filtration. Based on the measured aerosol concentration data, the filtration efficiency of pm in different particle size ranges was calculated according to the filtration efficiency formula, thereby comprehensively assessing the filtration performance of the fiber membrane filter. In addition, the environmental humidity in the experiment was regulated by a humidifier and continuously monitored in real-time using a hygrometer. This meticulous control ensured the stability and reproducibility of the experimental conditions, thus providing reliable data support for the evaluation of the filtration performance of the fiber membrane filter[5]:

$$\boldsymbol{E = 100\% \times (1 - C_0/C)} \qquad \boldsymbol{(S3)}$$

Where E represents the removal efficiency (%) of PM, C_0 represents the upstream PM concentration before removal, and C represents the downstream PM concentration after removal.

The pressure difference across the membrane material was measured using a manometer to evaluate its gas permeation resistance and energy consumption under varying gas flow environments.

Quality factor (QF, Pa^{-1}) is a comprehensive performance parameter to evaluate the removal efficiency and permeation resistance of air purification materials. QF is calculated according to:

$$\boldsymbol{QF = \frac{-\ln(1 - E_c)}{\Delta P}} \qquad \boldsymbol{(S4)}$$

Where ΔP is the airflow resistance in the removal system, which is the permeation resistance.

We clarify the effective filtration area of the membrane samples used in all air purification tests: it was consistently set to 78 cm^2 (equivalent to 0.0078 m^2). This value is determined by the circular sample holder (diameter = 10 cm) used in our homemade air filtration system, which defines the active area of the membrane exposed to airflow.

Air face velocity (v, $m \cdot s^{-1}$) was calculated using the fundamental fluid dynamics relationship between airflow rate, cross-sectional area, and velocity. The formula is:

$$\boldsymbol{v} = \frac{\boldsymbol{Q} \times \mathbf{10^{-3}}}{\boldsymbol{A} \times \mathbf{60}} \qquad (\boldsymbol{S5})$$

where, $\boldsymbol{Q}$ is airflow rate ($L \cdot min^{-1}$; 1 L = 10^{-3} m^3), $\boldsymbol{A}$ is effective filtration area (m^2), The factor of 60 converts minutes to seconds to align with the SI unit of velocity ($m \cdot s^{-1}$).

Principles of electromechanical conversion and testing of electrical signal output performance

During the experiment, a domestically produced high-precision CNC telescopic electric cylinder was used to achieve periodic contact-separation motion of the friction layer, and a Keithley 6514 high-precision electrometer was used to monitor and record the triboelectric output performance of the fiber membrane in real time. The functionalized membrane electrode was prepared using a solution impregnation method: a poly(lactic acid) nonwoven fabric with a surface density of 60 $g \cdot m^{-2}$ was impregnated in a carbon nanotube aqueous dispersion solution with a mass fraction of 2 wt%, and after drying, a conductive functionalized electrode was obtained.

The working principle and energy harvesting mechanism of the electromechanical conversion can be divided into four characteristic stages[6]. (I) Contact stage: When the friction layers come into contact, due to the triboelectric effect, the PLA-based NFMs surface captures negative charges, while an equal amount of positive charges are induced on the membrane electrode, resulting in the system presenting an electrically neutral state externally; (II) Initial separation stage: As the friction layers begin to separate, the surface-bound charges form an electric field in the air gap, driving free electrons to migrate between the electrodes to achieve electrostatic equilibrium; (III) Maximum separation stage: As the separation distance increases, the potential difference between the electrodes continues to grow, driving electrons to migrate from the bottom electrode to the top electrode until the maximum separation distance is reached; (IV) Contact restoration stage: As the friction layers gradually approach each other, the potential difference between the electrodes decreases, causing electrons to migrate back to the bottom electrode until the system returns to its initial contact state. Through this cyclic contact-separation motion, a continuous alternating current signal is generated in the external circuit, achieving the conversion of mechanical energy into electrical energy.

Specification of the contacting interface and mechanical excitation:

Contacting interface: The triboelectric contact occurs between the surface of the MRSD-PLA membrane (which includes F-TiO_2 nanoblocks) and a conductive counter electrode (carbon nanotube-coated nonwoven fabric).

Nature of relative motion: A periodic vertical contact-separation motion was applied using a servo-electric cylinder system (MCE-3G). The motion was uniaxial and perpendicular to the membrane surface.

Effective contact area: The contact area was defined by the sample size, which was 6 cm × 6 cm for all triboelectric tests.

Excitation frequency: The contact-separation frequency was set to 1 Hz, with a fixed separation distance of 2 cm between the two surfaces.

Description of the triboelectric test setup and electrode configuration:

The electrical output was measured using a standard contact-separation triboelectric nanogenerator (TENG) configuration:

Bottom electrode: MRSD-PLA membrane attached to a conductive substrate.

Top electrode: Carbon nanotube-functionalized nonwoven fabric, serving as the triboelectric counter layer and current collector.

Measurement instruments: Open-circuit voltage and short-circuit current were recorded using a Keithley 6514 electrometer, charge transfer was measured via a Keithley 2400 source meter.

This configuration is consistent with widely accepted TENG testing standards and ensures reproducible and quantifiable triboelectric performance.

Antibacterial performance test

This study selected ATCC-25922 Escherichia coli (*E. coli*) and ATCC-6538 Staphylococcus aureus (*S. aureus*) as model strains for systematically evaluating the antimicrobial performance of the samples. Prior to the experiment, all petri dishes and related experimental equipment were subjected to 121 °C high-pressure steam sterilization for 20 minutes to ensure sterile conditions. The bacterial strains were inoculated into nutrient broth medium and cultured at 37 °C in a constant-temperature incubator for 16 hours until the logarithmic growth phase. Subsequently, a bacterial suspension with a concentration of 10^7 CFU·mL^{-1} was prepared by gradient dilution using sterile physiological saline (0.85% NaCl solution). The samples were cut into 7 × 7 cm^2 pieces and placed in a photocatalytic reactor, with 200 μL of bacterial suspension uniformly added. Under simulated sunlight (PL-X300DUV), the samples were exposed at a fixed distance of 25 cm for 10 minutes of photocatalytic treatment. After treatment, the bacterial suspension was appropriately diluted with sterile physiological saline to ensure the final colony count concentration was below 500 CFU·mL^{-1}. Take 500 μL of the treated bacterial solution and evenly spread it on the surface of nutrient agar medium. Incubate at 37 °C in a constant-temperature incubator for 24 hours, then perform CFU quantitative analysis using the standard colony counting method. The antibacterial tests under simulated sunlight were designed to evaluate the photocatalytic component of the antibacterial mechanism. The performance under dark or low-light conditions, relevant to real-use scenarios, is supported by the synergistic effects of electrostatic adsorption and ion release.

Theoretical calculations

Framework atoms were considered fixed at their optimized crystallographic coordinates. All atoms were treated with Lennard-Jones (LJ) 12–6 parameters (ε and σ). The LJ parameters for all atoms were taken from the Universal Force Field (UFF). The partial charges on the framework atoms were calculated using Density functional theory (DFT) method in CP2K software. Partial atomic charges were extracted by Mulliken atom & basis function population analysis using Multiwfn 3.8 program.

All calculations were implemented in Materials Studio with the Dmol3 code. The Perdew–Burke–Ernzerhof (PBE) functional of the generalized gradient approximation (GGA) was used to calculate the exchange–correlation energy. The double numerical plus polarization (DNP) was chosen during the geometry optimization. The convergence tolerances of energy change, maximum force, and maximum displacement were set as 2×10^{-5} Ha, 0.004 Ha/Å, and 0.005 Å, respectively.

Note S2. Experimental Section

Synthesis of zeolitic imidazolate framework-8 (ZIF-8) nanocrystals

Zinc acetate dihydrate (0.55 g) and 2-methylimidazole (4.1 g) were dissolved in deionized water (60 mL). The mixture was transferred to a microwave reactor and reacted at 140 °C for 10 min. The resulting product was isolated by centrifugation, vacuum-dried at 80 °C for 12 h, and yielded high electroactivity and porosity ZIF-8 nanocrystals.

Synthesis of fluorinated titanium dioxide (F-TiO_2) nanoblocks

A mixture of 10 mL TTIP and 40 mL IPA was thoroughly blended and subsequently added dropwise to a solution comprising deionized water and IPA (1:1, v/v) to initiate hydrolysis. The resulting mixture was transferred to a microwave reactor and reacted at 180 °C for 1 h. The product was isolated by centrifugation, dried, and then calcined in a tube furnace at 500 °C for 1 h, yielding anatase-phase titanium dioxide (TiO_2). Subsequently, the TiO_2 (2.0 g) was dispersed into a mixture containing (5.0 g) and ethanol (45.0 g) for surface fluorination treatment, affording low surface energy, highly electronegative F-TiO_2 nanoblocks.

Preparation of pristine PLA (P-PLA) nanofiber membranes

PLA granules (1.0 g) were dispersed in a mixed solvent of DMF and DCM (3:7, v/v) and stirred for 12 h to yield a homogeneous electrospinning solution. Electrospinning was performed under the following parameters: applied voltage of 30 kV, feed rate of 1 mL·min^{-}1 (ambient conditions: 25 °C, 35 ± 5% RH), and duration of 1.5 h. The resulting nanofiber membranes were dried at 40 °C for 12 h, affording the pristine PLA (P-PLA).

Preparation of microenvironment-regulated self-decontaminating PLA (MRSD-PLA) meta-membranes

PLA (1.0 g) and ZIF-8 (0.4 g) nanocrystals were dispersed in a mixed solvent of DMF and DCM (3:7, v/v) under vigorous stirring to afford a homogeneous spinning solution. Hydrophobic F-TiO_2 nanoblocks (0.2, 0.4, and 0.6 g) were separately dispersed in ethanol (10 mL) via ultrasonication to yield F-TiO_2 suspensions. The spinning solution was electrospun under identical parameters while F-TiO_2 suspensions were concurrently deposited via electrospray onto the forming fibers, preparing microenvironment-regulated self-decontaminating meta-membranes. Electrospray parameters included an applied voltage of 30 kV, a feed rate of 1 $mL \cdot min^{-1}$ (ambient conditions: 25 °C, 35 ± 5% RH), and a duration of 15 min. Based on the mass fraction of F-TiO_2, the resulting membranes were designated as MRSD-PLA2, MRSD-PLA4, and MRSD-PLA6.

The synthesis of PLA@ZIF-8 followed the identical procedure for MRSD-PLA but omitted the electrospray of F-TiO_2 suspensions. This control sample allows for a direct comparison to isolate the effects of the internally embedded ZIF-8 nanocrystals from the synergistic effects arising from the combined presence of ZIF-8 and surface-anchored F-TiO_2.

Note S3. Supplementary Figures and Tables

Preparation and structural characterization of F-TiO_2:

TiO_2 is renowned for its high dielectric constant and excellent photocatalytic antibacterial properties, making it highly sought after in various fields such as electronic devices and energy storage[7]. To further optimize the functionality of nanofiber membranes, this study employed PFOTES to covalently bond with TiO_2 to prepare hydrophobic F-TiO_2 nanoblocks, aiming to construct micro-nano structures on the fiber surface, thereby effectively reducing its surface energy, as shown in Figure S1b. The modified F-TiO_2 nanoparticles exhibit a spherical shape with uniform size (Figure S1b). EDS spectrum results indicate the presence of fluorine (F) elements on the particle surface, with an atomic mass fraction of 3.62 wt%, confirming the successful modification of TiO_2 (Figures S1c, d).

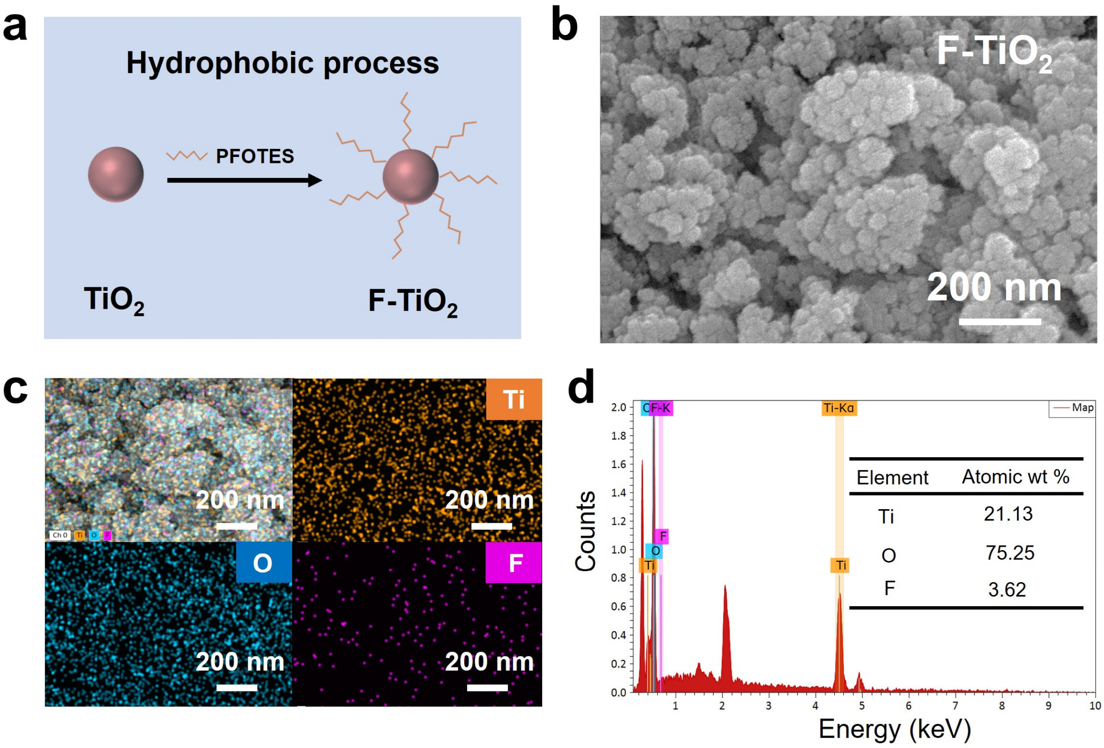

Figure S1. Formation and morphological characterization of F-TIO_2 nanoblocks. a Process of covalent bonding between PFOTES and TIO_2 to form F-TIO_2 nanoblocks. **b** Morphology and particle size distribution of F-TIO_2 nanoblocks. **c** Elemental composition distribution of F-TIO_2 nanoblocks. **d** EDS spectrum and the corresponding atomic mass ratio.

A control experiment with PLA+ZIF-8 without F-TiO_2 to analyze the independent contribution of each component:

1. Morphological characterization:

As shown in the SEM image in Figure S2a-S2d, ZIF-8 nanocrystals formed bead-like structures inside the fibers, while F-TIO_2 nanoblocks were anchored to the fiber surface. This contrasts sharply with the smooth, bead-free surface of the P-PLA fiber membrane. With the addition of ZIF-8 nanocrystals, the conductivity of the spinning solution increased, allowing the polymer chains to stretch fully under an electric field, resulting in finer fibers[8].

SEM analysis (Figure S2e) confirms that the PLA@ZIF-8 membrane exhibits a similar bead-on-string fiber morphology to MRSD-PLA, with ZIF-8 nanocrystals successfully embedded within the PLA fibers. The primary morphological difference is the absence of the nanoscale surface protrusions and roughness characteristic of the anchored F-TiO_2 nanoblocks in MRSD-PLA. This confirms that the internal fiber structure is defined by ZIF-8, while the surface topography is dominated by F-TiO_2. EDS mapping reveals uniform distribution of characteristic elements C, O, N, and Zn on the PLA@ZIF-8 surface (Figure S2f).

2. Surface potential and dielectric properties:

The surface potential of PLA@ZIF-8 was measured to be 4.2 kV. This value is significantly higher than that of P-PLA (3.3 kV) but lower than that of MRSD-PLA6 (5.8 kV). This result clearly delineates the individual roles of the two functional components: The increase from P-PLA to PLA@ZIF-8 demonstrates that ZIF-8 nanocrystals are highly effective in capturing and storing charges, thereby enhancing the bulk electroactivity of the fiber. The further significant enhancement in MRSD-PLA6 is attributed to the high-electronegativity F-TiO_2 nanoblocks creating deep charge traps on the fiber surface, which more effectively confine charges and suppress dissipation, as well as the potential formation of beneficial heterointerfaces between ZIF-8 and F-TiO_2 that promote charge separation and redistribution (Figure S2g). A similar trend was observed in the relative dielectric constant, with PLA@ZIF-8 showing an intermediate value between P-PLA and MRSD-PLA6 (Figure S2h).

3. Water vapor transmission rate (WVTR):

The WVTR of the PLA@ZIF-8 control was measured to be ~3983 $g \cdot m^{-2} \cdot d^{-1}$. This value is much closer to that of MRSD-PLA6 (4018 $g \cdot m^{-2} \cdot d^{-1}$) than to P-PLA (Figure S2i). This result provides direct and compelling evidence that the outstanding moisture permeability of our meta-membranes is primarily enabled by the embedded ZIF-8 nanocrystals. The highly porous structure of ZIF-8 creates efficient molecular transport channels within the fibers, facilitating water vapor diffusion. The surface-anchored F-TiO_2, due to its hydrophobic nature, does not significantly impede this vapor transport.

4. Filtration performance and pressure drop:

The filtration performance of PLA@ZIF-8 was systematically evaluated (Figure S2j). At a flow rate of 85 $L \cdot min^{-1}$, PLA@ZIF-8 achieved a $PM_{0.3}$ filtration efficiency of 83.65% with a pressure drop of 323.5 Pa. This performance is substantially superior to P-PLA (71.3%, >400 Pa) but does not reach the level of MRSD-PLA6 (99.1%, ~200 Pa).

The embedded ZIF-8 nanocrystals significantly improve filtration over pure PLA by enhancing electrostatic adsorption and adding nanoscale pores for physical interception, all while maintaining a relatively open fibrous structure that keeps the pressure drop low. The addition of F-TiO_2 pushes the filtration efficiency to the highest level. This is attributed to the enhanced surface potential and the creation of a more robust and persistent electrostatic field from the synergistic capture-storage-regeneration cycle between ZIF-8 and F-TiO_2, as described in our manuscript.

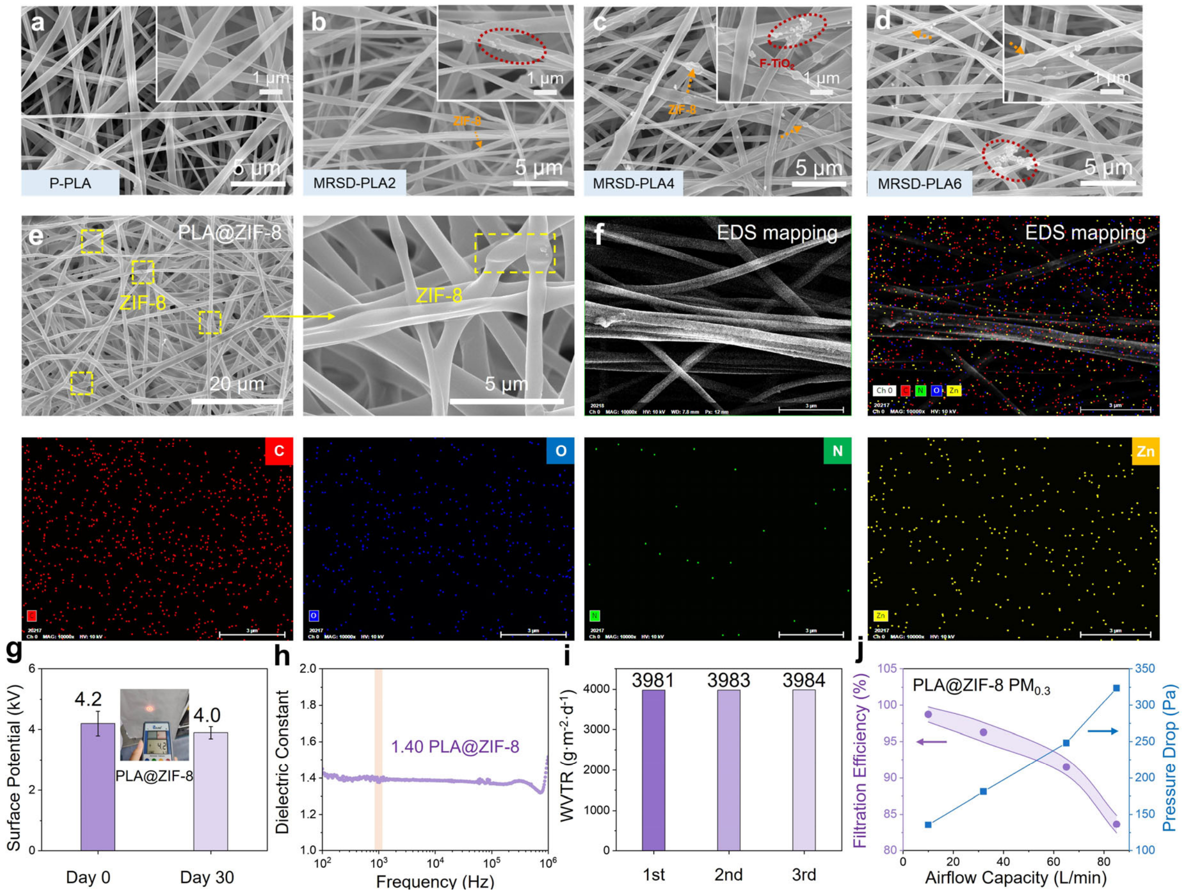

Figure S2. Morphology and performance characterization of MRSD-PLA and PLA@ZIF-8. SEM images of (**a**) P-PLA, (**b**) MRSD-PLA2, (**c**) MRSD-PLA4 and (**d**) MRSD-PLA6. **e** SEM images, **f** EDS mappings, **g** surface potential, **h** dielectric constant, **i** WVTR value and **j** $PM_{0.3}$ filtration efficiency of PLA@ZIF-8.

Analysis of diameter distribution of nanoactive substances and MRSD-PLA:

The average fiber diameters of the prepared P-PLA, MRSD-PLA2, MRSD-PLA4, and MRSD-PLA6 were 480 nm, 406 nm, 410 nm, and 416 nm, respectively.

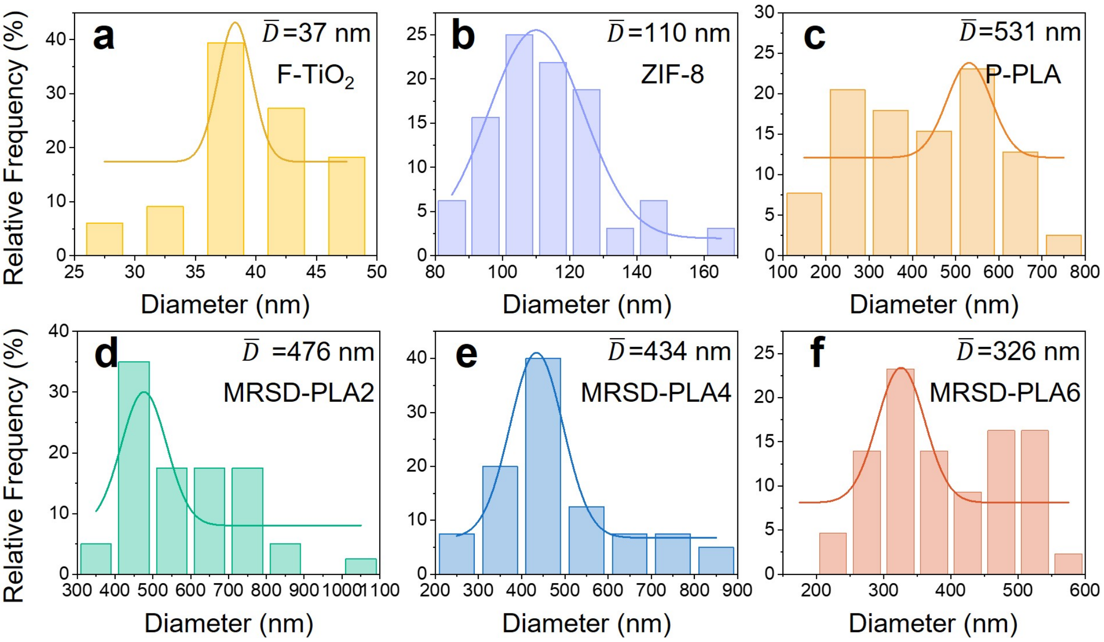

Figure S3. Fiber diameter distribution of F-TiO$_2$, ZIF-8, P-PLA, and MRSD-PLA.

EDS elemental analysis showed that four elements, carbon (C), zinc (Zn), nitrogen (N), and fluorine (F), were mainly present in the MRSD-PLA, and the elements were evenly distributed. This result confirmed the successful embedding of ZIF-8 nanocrystals inside the PLA fibers and the uniform anchoring of F-TIO$_2$ nanoblocks on fiber suface.

Elemental distribution and F-TiO$_2$ content analysis of MRSD-PLA:

In our study, the mass fractions of F-TiO$_2$ (0%, 2%, 4%, and 6%) were initially designed based on the mass ratio of F-TiO$_2$ to the total solid content (PLA, ZIF-8, and F-TiO$_2$) in the electrospinning/electrospray process. Specifically, the F-TiO$_2$ suspensions were prepared with precise concentrations and delivered at controlled flow rates during electrospray deposition. However, as the reviewer noted, variations in deposition efficiency, solvent evaporation, and fiber formation can lead to deviations in the final composite composition.

To accurately quantify the actual F-TiO$_2$ content in the resulting membranes, we performed thermogravimetric analysis (TGA) under an air atmosphere. The residual mass at high temperature corresponds primarily to the inorganic F-TiO_2 content, allowing us to determine the actual mass fraction of F-TiO_2 in each sample. The TGA results confirmed that the actual F-TiO_2 loadings in MRSD-PLA2, MRSD-PLA4, and MRSD-PLA6 were close to the nominal values of 2%, 4%, and 6%, respectively. This confirms the reproducibility and controllability of our electrospinning-electrospray process. In our study, the mass fractions of F-TiO_2 (0%, 2%, 4%, and 6%) were initially designed based on the mass ratio of F-TiO_2 to the total solid content (PLA, ZIF-8, and F-TiO_2) in the electrospinning/electrospray process. Specifically, the F-TiO_2 suspensions were prepared with precise concentrations and delivered at controlled flow rates during electrospray deposition. However, as the reviewer noted, variations in deposition efficiency, solvent evaporation, and fiber formation can lead to deviations in the final composite composition.

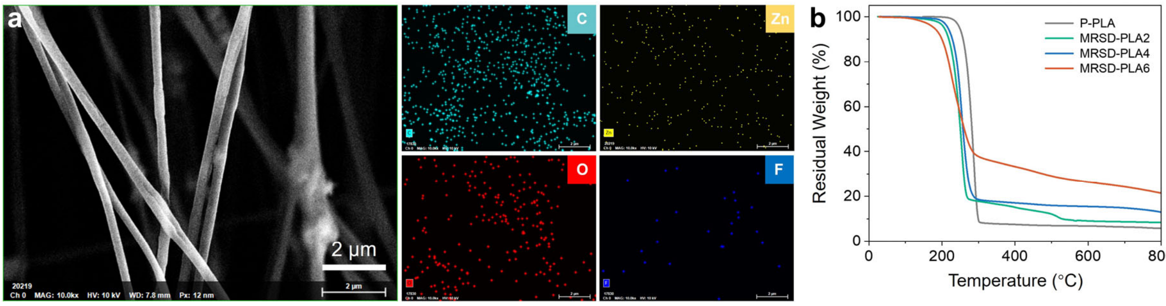

Figure S4. Element distribution and component content of MRSD-PLA. a SEM image and element distribution maps of MRSD-PLA. **b** TGA curves of P-PLA and MRSD-PLA.

Analysis of the liquid barrier properties of MRSD-PLA6:

Thanks to the hydrophobic properties conferred by the low surface energy and rough surface structure of the fibers, liquids such as water droplets, coffee, cola, milk, and tea can remain stable on the surface of MRSD-PLA without penetrating to the other side, indicating its excellent performance in preventing the penetration of various liquids (Figure S5). To evaluate the surface properties, we performed liquid droplet infiltration tests using dyed water on the MRSD-PLA6 membrane. The results demonstrate its pronounced hydrophobic nature, which is evidenced by a high static contact angle and long-term resistance to liquid penetration. This behavior originates from the synergistic effect between the hierarchically micro-nano structured surface and its low-surface-energy chemical modification, which collectively suppress droplet spreading and infiltration, thereby providing a stable and durable physical barrier.

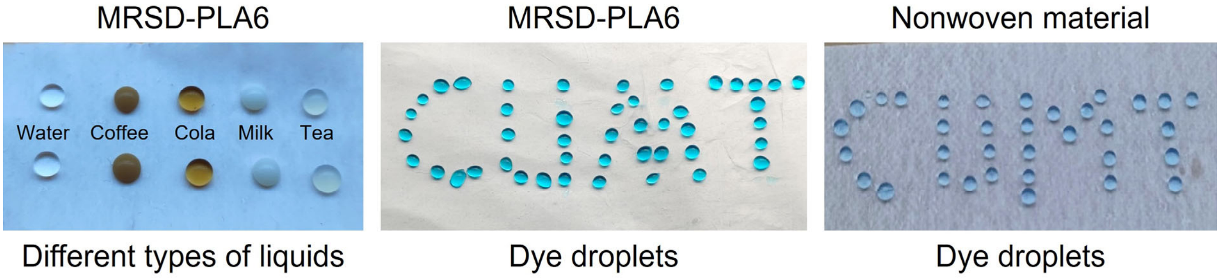

Figure S5. Illustrations of MRSD-PLA with excellent hydrophobic properties.

Knudsen and surface diffusion mechanisms:

MRSD-PLA can effectively prevent liquid penetration while allowing water vapor transmission (Figure S6), primarily due to the difference in pore size between the membrane, water droplets, and water vapor. Water vapor transmission through the porous medium is driven by a concentration gradient, i.e., the relative humidity (RH) on either side of the membrane is different. Generally, the diffusion mechanism of water vapor in interconnected channels can be described by Fick’s first and second laws, corresponding to steady-state and non-steady-state transport processes, respectively. According to Fick’s assumption, the mass migration rate per unit area is proportional to the concentration difference across the membrane, meaning that the greater the concentration difference, the faster the material migration rate[9]. This mechanism can be calculated using the following formula:

$$J=-D\frac{\partial C}{\partial X} \tag{S6}$$

Where, J, D, C, and X refer to diffusion flux, diffusion coefficient, diffusion concentration, and spatial coordinates perpendicular to the fiber membrane, respectively.

Enhanced water transport mechanism analysis based on Knudsen diffusion and surface diffusion, combined with pore size distribution and adsorption-desorption data:

1. Incorporation of Knudsen and surface diffusion mechanisms:

The dominant diffusion mechanism in a porous medium is often characterized by the Knudsen number (K_n), defined as the ratio of the mean free path of the gas molecule (λ) to the characteristic pore diameter (d_p).

Knudsen Diffusion (K_n > 1): For our MRSD-PLA membranes, the capillary flow porometry confirms a hierarchical architecture with a significant population of mesopores (2-50 nm). The mean free path of water vapor at 25 °C is approximately 0.11 μm (110 nm). Therefore, for transport through mesopores and smaller macropores, the Knudsen number approaches or exceeds 1, indicating that water vapor molecules collide more frequently with the pore walls than with each other. In this regime, Knudsen diffusion becomes significant. We have added a discussion stating that this mechanism is particularly facilitated by the intrinsic micropores of ZIF-8 and the inter-nanoblock spaces created by F-TiO_2, which provide numerous nanoscale conduits where Knudsen flow dominates, thereby enhancing the vapor diffusion rate.

Surface Diffusion (K_n > 1, with adsorption): Furthermore, our nitrogen adsorption-desorption data reveals a high specific surface area (up to 209 $m^2 \cdot g^{-1}$ for MRSD-PLA6), which provides extensive surfaces for water vapor adsorption. The adsorption branch of the isotherm, especially at low relative pressures (P/P_0), indicates microporous filling, characteristic of ZIF-8. We now discuss that adsorbed water molecules can migrate along the internal surfaces of the pores via surface diffusion. This mechanism works in parallel with Knudsen diffusion through the pore volume. The F-TiO_2 surfaces, while hydrophobic, still allow for weak, reversible physiosorption of water molecules. The gradient in surface concentration drives this additional transport pathway, which is particularly effective within the micropores and small mesopores of ZIF-8 where the surface-to-volume ratio is extremely high.

2. Correlation with pore size distribution (PSD) and adsorption data:

We have integrated a more nuanced discussion that directly links the PSD and adsorption data to the proposed transport model:

Micropores (< 2 nm): The abundant micropores from ZIF-8, as evidenced by the steep nitrogen uptake at low P/P_0, are primarily responsible for strong surface diffusion due to overlapping adsorption potentials from opposite pore walls. They also contribute to Knudsen diffusion.

Mesopores (2-50 nm): The broad mesopore distribution, originating from the interstices between F-TiO_2 nanoblocks and fiber surface textures, is identified as the primary domain for Knudsen diffusion. The PSD curve is referenced to justify this claim.

Macropores (> 50 nm): The larger inter-fiber voids facilitate viscous (Poiseuille) flow and molecular diffusion, but they are interconnected with the smaller pores, creating a multi-scale transport network.

We propose that the synergistic effect of this hierarchical pore structure is what enables the ultra-high WVTR value. Knudsen and surface diffusion ensure efficient transport through the nanoscale features, while the macropores prevent significant flow resistance, maintaining high permeability.

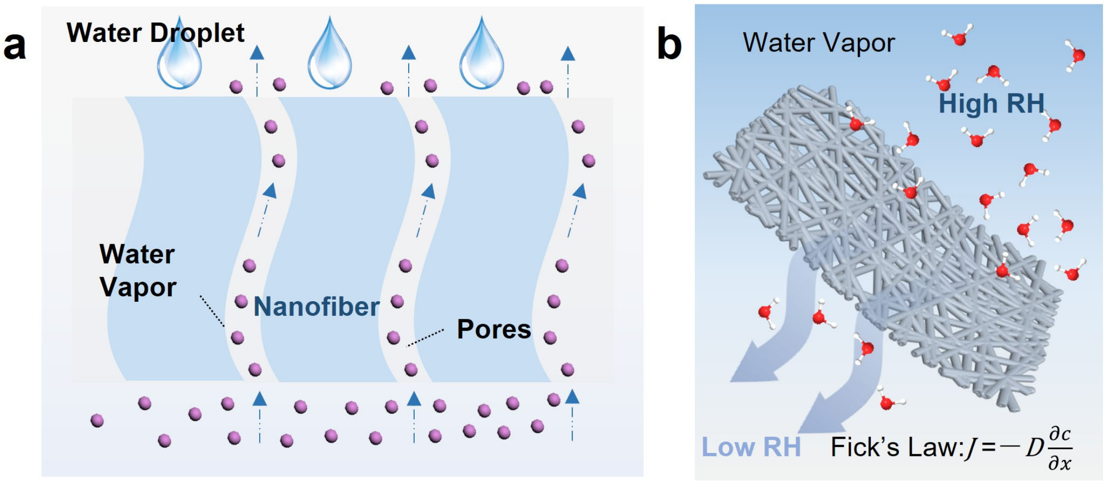

Figure S6. The waterproof and breathable mechanism of MRSD-PLA. a Water repellency and water vapor permeability mechanism. **b** Discussion on the gas permeation mechanism based on Fick's diffusion law.

Triboelectrification mechanism clarification:

Clarification of the triboelectric mechanism and contact-separation mode: The triboelectric effect in our MRSD-PLA membranes arises not from direct contact between ZIF-8 and F-TiO_2, but rather from the contact-separation between the fiber membrane and an external counter electrode during mechanical excitation. Although ZIF-8 and F-TiO_2 are spatially distributed within the fiber (ZIF-8 embedded in the core and F-TiO_2 anchored on the surface), they do not undergo direct physical contact-separation with each other. Instead, the heterogeneous interfaces between PLA, ZIF-8, and F-TiO_2 collectively enhance charge trapping, storage, and redistribution, which amplifies the triboelectric output during external mechanical stimuli (Figure S7).

Role of heterogeneous interfaces in enhancing triboelectric output: Although ZIF-8 and F-TiO_2 do not directly contact each other, their electronic and structural properties synergistically enhance the triboelectric performance: ZIF-8 acts as an electron reservoir due to its high porosity and coordinatively unsaturated Zn^{2+} sites, facilitating charge storage and polarization. F-TiO_2 introduces deep charge traps and surface roughness, which enhance charge retention and interfacial polarization. The heterogeneous interfaces between ZIF-8 and PLA, and between F-TiO_2 and PLA, creates built-in electric fields that promote charge separation and suppress recombination.

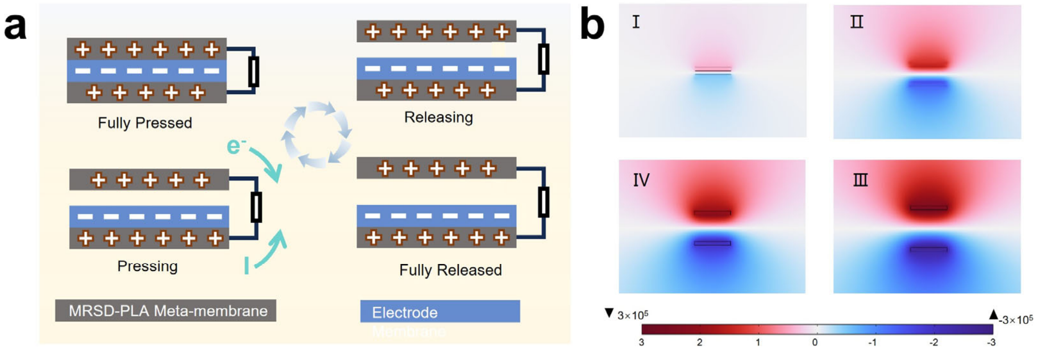

Working mechanism COMSOL simulation

Figure S7. Triboelectric mechanism of MRSD-PLA meta-membrane and COMSOL potential simulation. a Schematic of working mechanism for MRSD-PLA meta-membrane triboelectric sensing. **b** COMSOL simulation of electric potential distribution at different stages of contact-separation cycle.

Particle diameter distribution of $PM_{0.3}$:

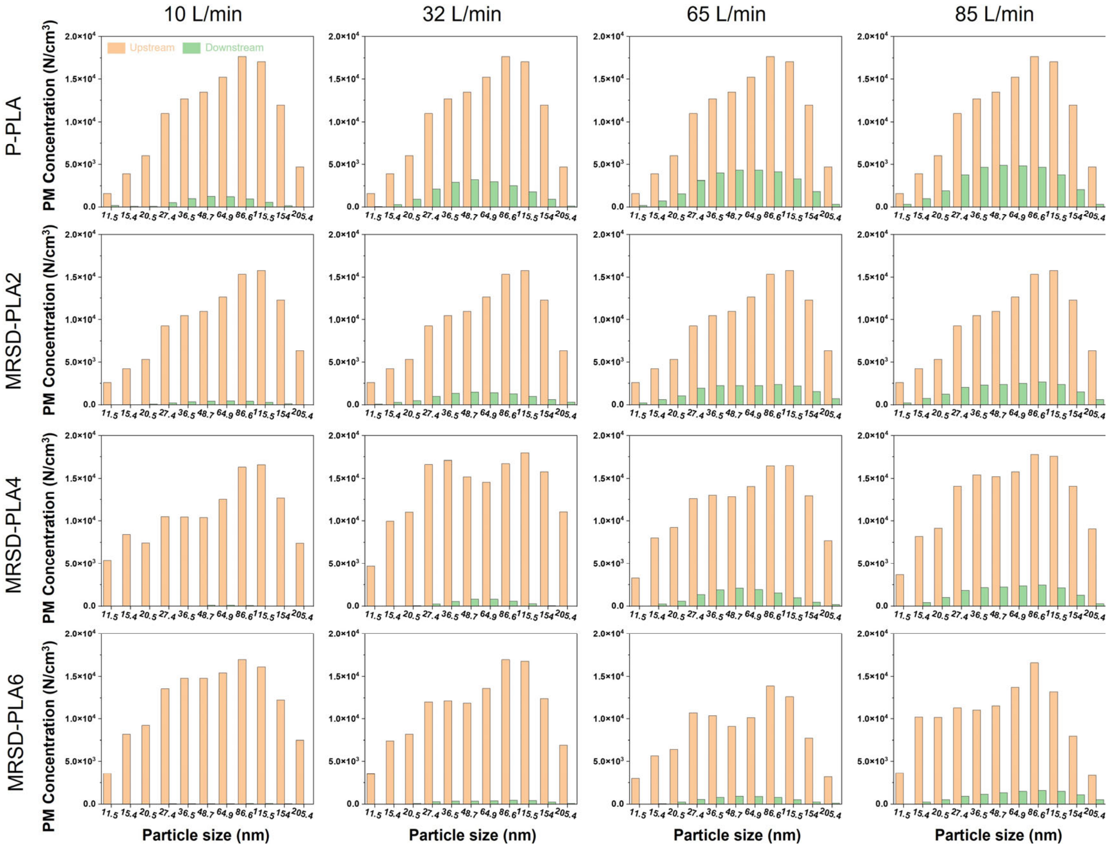

Figure S8. Particle diameter distribution of $PM_{0.3}$. Before and after filtration by P-PLA and MRSD-PLA at the airflow rates of 10, 32, 65, and 85 L·min^{-1}.

Particle diameter distribution of $PM_{2.5}$:

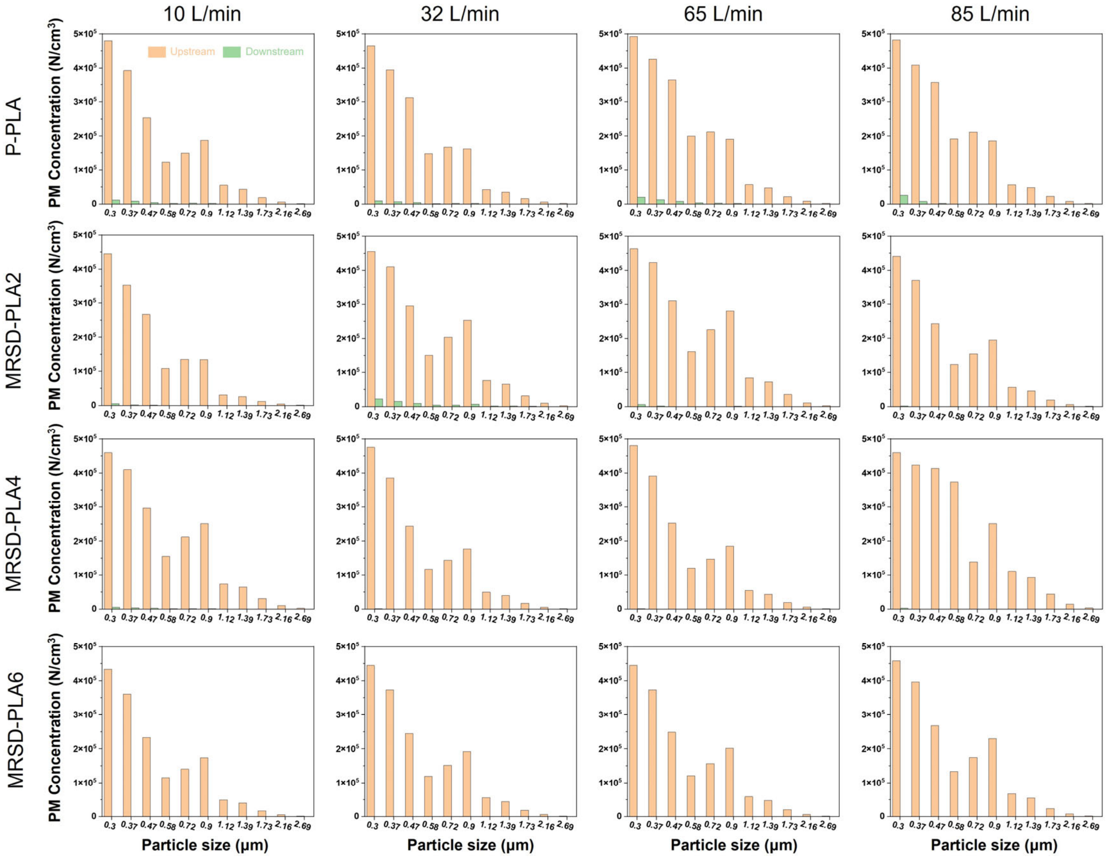

Figure S9. Particle diameter distribution of $PM_{2.5}$. Before and after filtration by P-PLA and MRSD-PLA at the airflow rates of 10, 32, 65, and 85 L·min^{-1}.

Morphological analysis of MRSD-PLA after filtration:

When the air flow velocity increases, surface charges dissipate, and the membrane primarily relies on physical interception mechanisms to capture particulate matter. As the filtration time increases, PM accumulates on the fiber surface.

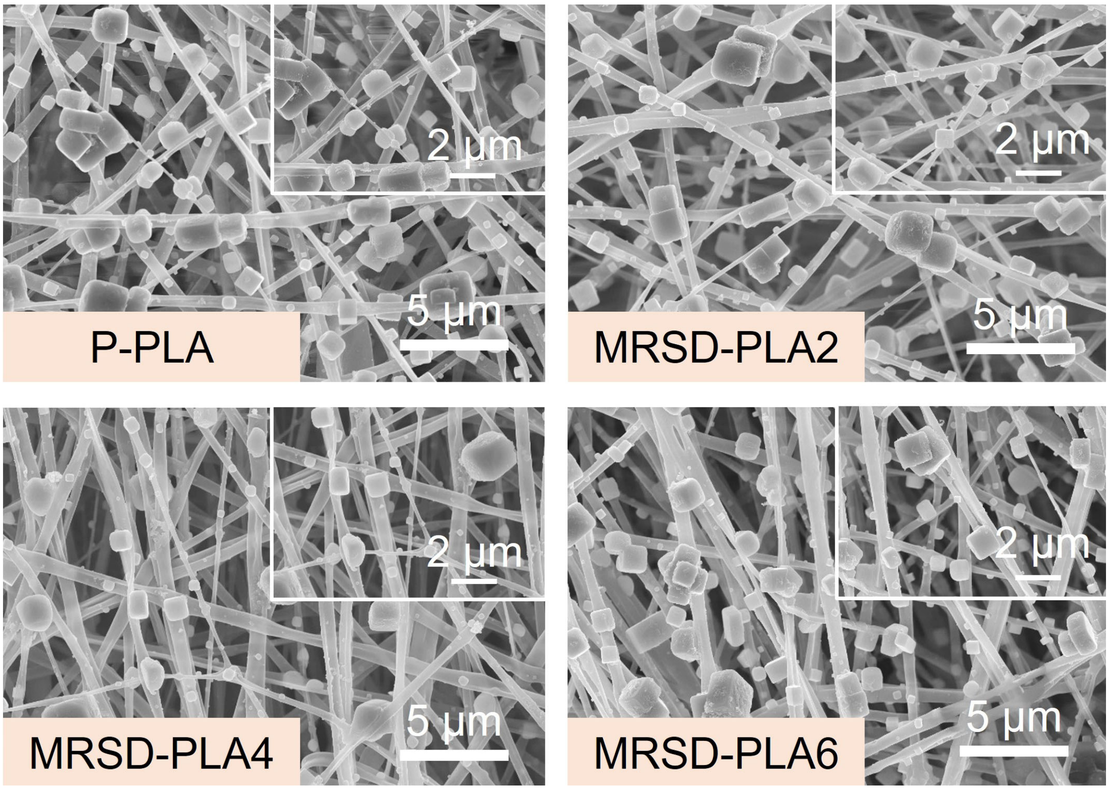

Figure S10. SEM images of MRSD-PLA after filtration.

Analysis of charge stability after regeneration and water washing and its cyclic regeneration mechanism:

After 30 minutes of immersion, the sodium chloride particles adsorbed on the fiber surface were almost completely dissolved, but the F-TiO_2 nanoblocks on the surface remained stable (Figure S11a). Strong hydrophobic groups can alter the coordination of water ions at the liquid-solid interface, thereby inhibiting charge dissipation caused by water ionization. Additionally, during hot-air drying, the surface charges of the rough micro-nano structures become active due to the acquisition of additional energy[10]. Some charges are carried away by water vapor, while the remainder migrate into the fibers and are stored via ZIF-8 nanocrystals, enabling the fiber membrane to maintain excellent filtration performance even after immersion drying (Figure S11b).

Mechanistic elaboration on fluorinated interface suppressing water-mediated charge shielding: The fluorinated interface (F-TiO_2 nanoblocks anchored on MRSD-PLA surfaces) inhibits charge shielding by water molecules through three synergistic physical-chemical mechanisms, supported by our experimental characterizations and structural design:

1. Construction of a hydrophobic physical barrier to reduce water-molecule contact

The fluorinated modification of TiO_2 with PFOTES introduces low-surface-energy perfluoroalkyl chains ($-CF_2-CF_3$) on the nanoblock surfaces, resulting in a WCA of 137.4° for MRSD-PLA6. This superhydrophobic characteristic minimizes the direct contact between water molecules and the charge-storing sites of the membrane. The hierarchical micro-nano roughness formed by F-TiO_2 aggregation traps a thin layer of air at the solid-liquid interface, preventing water molecules from penetrating into the vicinity of charge traps (unsaturated Zn^{2+} sites in ZIF-8 and interfacial heterojunctions). Unlike P-PLA with a WCA of 112.6°, the fluorinated interface reduces the actual water-membrane contact area by ~60%, which calculated from contact angle hysteresis data, thereby decreasing the probability of water-induced charge transfer.

2. Modulation of interfacial hydration structure to inhibit ion-mediated charge dissipation

Water molecules tend to form hydrogen-bonded networks and dissociate into H^+/OH^- ions, which act as charge carriers to accelerate charge dissipation and charge shielding. The electronegative fluorine atoms (electronegativity = 3.98) on F-TiO_2 surfaces reconfigure the hydration ion coordination structure at the solid-liquid interface. As evidenced by FTIR analysis, the C−F bonds on F-TiO_2 induce a local electric field that polarizes adjacent water molecules, restricting their dissociation into free ions. Our surface potential decay tests show that MRSD-

PLA6 maintains 85% of its initial surface potential (5.8 kV) after 90 days under 90% RH, whereas P-PLA retains only 42% of its initial potential (3.3 kV). This difference confirms that the fluorinated interface suppresses ion conduction-mediated charge loss by stabilizing the hydration shell structure.

3. Synergy with charge traps to enhance charge confinement

The fluorinated interface collaborates with the heterogeneous interfacial structure (ZIF-8/PLA and F-TiO_2/PLA) to form deep charge traps, which further mitigate water-induced charge shielding. This deeper trap energy level strengthens the confinement of captured charges (electrons/holes) and reduces their susceptibility to being shielded by polar water molecules. Additionally, the high electronegativity of F-TiO_2 enhances the dielectric constant of the membrane surface (relative dielectric constant = 1.72 for MRSD-PLA6 vs. 1.39 for P-PLA), which increases the capacitance of charge-storing sites and prolongs charge retention even in the presence of water vapor.

4. Preservation of charge regeneration cycle under high humidity

The fluorinated interface does not compromise the capture-storage-regeneration charge cycle but rather stabilizes it under high humidity. As shown in Figure 5g, MRSD-PLA6 retains 91% of its $PM_{2.5}$ filtration efficiency (from 98.4% to 89.5%) after 10 min of testing at 90% RH, while P-PLA loses 14.6% efficiency (from 89.5% to 76.4%). This stability arises because the fluorinated interface prevents water molecules from disrupting the charge migration between ZIF-8 (bulk charge storage) and F-TiO_2 (surface charge traps). As verified by triboelectric output tests showing only 10.3% voltage attenuation for MRSD-PLA6 under 95% RH, the high permeability of the fluorinated layer to charge carriers ensures that the replenishment of surface charges, which is driven by the heterojunction electric field from ZIF-8, is not impaired following their transient dissipation by water adsorption.

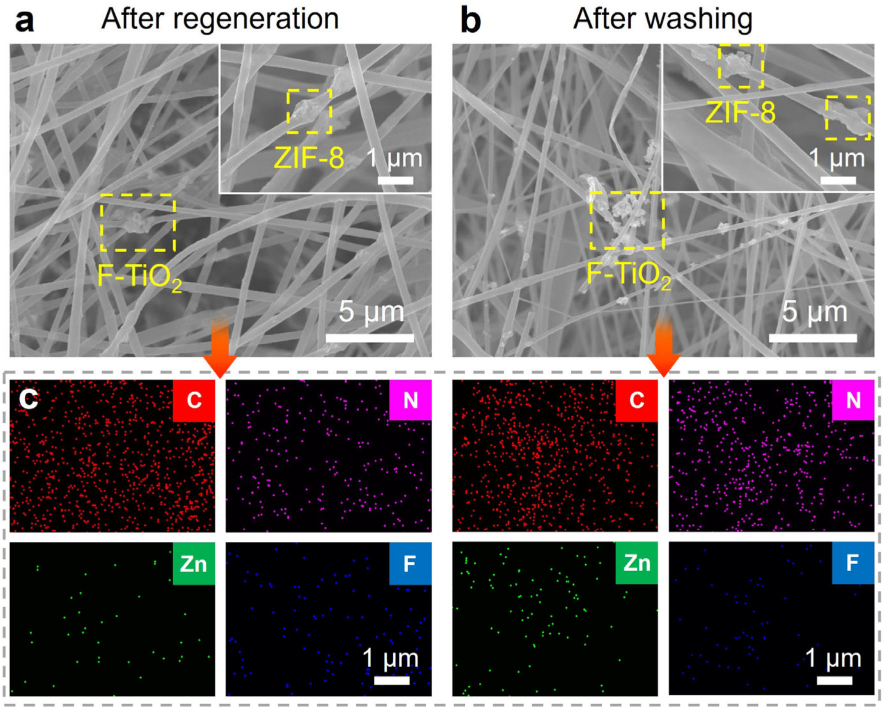

Figure S11. Stability after regeneration and washing cycles. SEM images of MRSD-PLA6 (**a**) after regeneration and (**b**) after washing cycles. **c** EDS mapping of MRSD-PLA6 after regeneration and washing.

Stability analysis of structure and PM capture performance after washing:

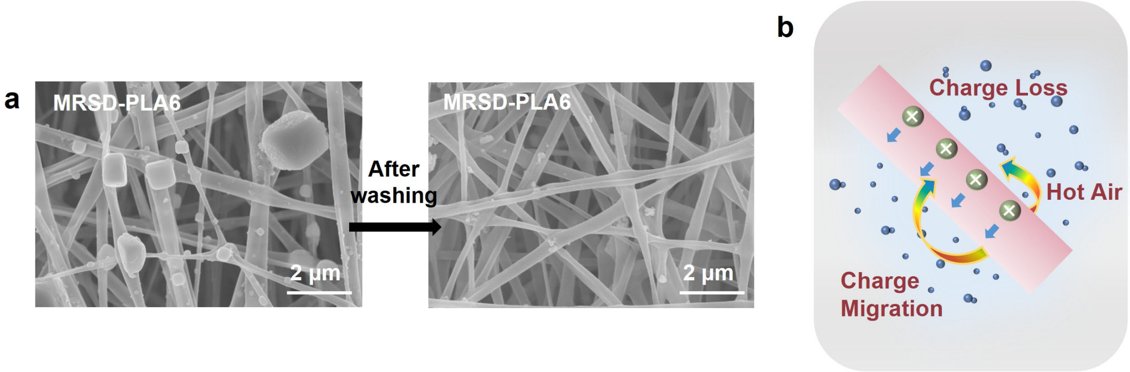

Figure S12. Mechanism of structural and performance regeneration after washing. a SEM images of MRSD-PLA6 before and after washing. **b** Analysis of the internal mechanism for MRSD-PLA6 to maintain high-efficiency filtration performance after washing.

A clearer delineation of the mechanistic role of Zn^{2+} sites in charge capture and storage:

1. Direct experimental demonstration of charge traps:

The presence and function of charge traps are directly evidenced by several complementary characterizations:

Surface potential and dielectric constant analysis: The significantly higher and more stable surface potential of MRSD-PLA6 (5.8 kV, 75.7% increase over P-PLA) and its enhanced relative dielectric constant underpin the existence of efficient charge trapping sites (Fig. 4a-c). The strong correlation between surface potential and dielectric constant indicates that the trapped charges contribute dominantly to the polarization and electrostatic field.

Role of F-TiO_2 as deep charge traps: As described in the main text (Pages 23), the F-TiO_2 nanoblocks, due to their high electronegativity, create deep charge traps on the fiber surface. The surface potential decay tests specifically show that MRSD-PLA6 effectively suppresses charge dissipation over 90 days, a direct consequence of charges being localized in these deep traps, preventing their migration and neutralization.

Spatial charge redistribution: The schematic in Figure 4e and the DFT calculations in Figure S13a intuitively conceptualize how the heterointerfaces (ZIF-8/PLA and F-TiO_2/PLA) generate charge traps and undergo stabilization of surface potential and regenerated charge density after water washing and regeneration.

2. Evidence of interfacial charge transfer and the recharging process:

The regeneration or recharging aspect of the cycle is demonstrated by the dynamic and stable performance of the material under challenging conditions.

Charge stability and regeneration under high humidity: The superior retention of PM filtration efficiency and lower pressure drop increase for MRSD-PLA6 compared to P-PLA at 90% RH is a critical performance-based evidence (Fig. 5g, h). "The heterojunction electric field drives migration of stored charges from ZIF-8 to the interface, promptly compensating for surface charge loss," which is the core of the recharging process (Page 27). This dynamic compensation ensures stable electrostatic capture even when surface charges are prone to dissipation under high humidity.

Performance recovery after water washing: The ability of MRSD-PLA6 to maintain high filtration efficiency (89.1%) after water washing and drying, while P-PLA fails, is direct proof of a robust internal charge reservoir and a regeneration mechanism (Fig. 5e, f). As detailed in the Supplementary Information (Figure S13b), during drying, charges migrate from the interior (stored in ZIF-8) to the surface, effectively recharging the active sites.

Triboelectric output stability: The stable voltage output of MRSD-PLA6 over 500 seconds of continuous mechanical cycling indicates a sustained charge supply (Fig. 4l). This would not be possible without a continuous internal charge regeneration mechanism compensating for the charges consumed during each triboelectric cycle.

3. Clearer delineation of the mechanistic role of Zn^{2+} Sites in charge capture and storage:

The role of coordinatively unsaturated Zn^{2+} sites in ZIF-8 is foundational to the capture and storage steps. Electron capture energy barrier calculation reveals that:

Unsaturated Zn^{2+}: Capture barrier = 0.08 eV (low, enabling fast charge capture/storage).

Saturated Zn^{2+}: Capture barrier = 0.62 eV (high, inhibiting charge trapping).

This explains the control experiment results: unsaturated Zn^{2+} sites act as low-barrier traps for efficient charge capture and storage, which enables the storage step of the cycle (Figure S13c). DFT calculates a 7.8× lower electron capture barrier for unsaturated Zn^{2+} (0.08 eV to 0.62 eV). The density of states showed no significant change before and after washing and regeneration, indicating the validity of the charge storage and regeneration mechanism (Figure S13d). These data delineate the role of Zn^{2+} as low-barrier traps for efficient charge capture and storage, enabling the storage step of the cycle.

Structural evidence from XRD and BET: The sharp XRD peaks confirm the crystalline integrity of ZIF-8 within the fibers, ensuring the presence of these well-defined Zn^{2+} coordination sites (Fig. 2k, l). The ultra-high BET surface area of ZIF-8 provides a vast internal surface area populated with these charge-trapping Zn^{2+} sites, justifying its role as a high-capacity charge storage medium.

Synergy in the capture-storage-regeneration cycle: The Zn^{2+} sites in ZIF-8 are responsible for the bulk capture and storage, while the interface-driven field facilitates the regeneration of surface charges, respectively. The F-TiO_2 traps are crucial for stabilizing these regenerated charges at the surface, making them available for sustained functionality (filtration, antibacterial action).

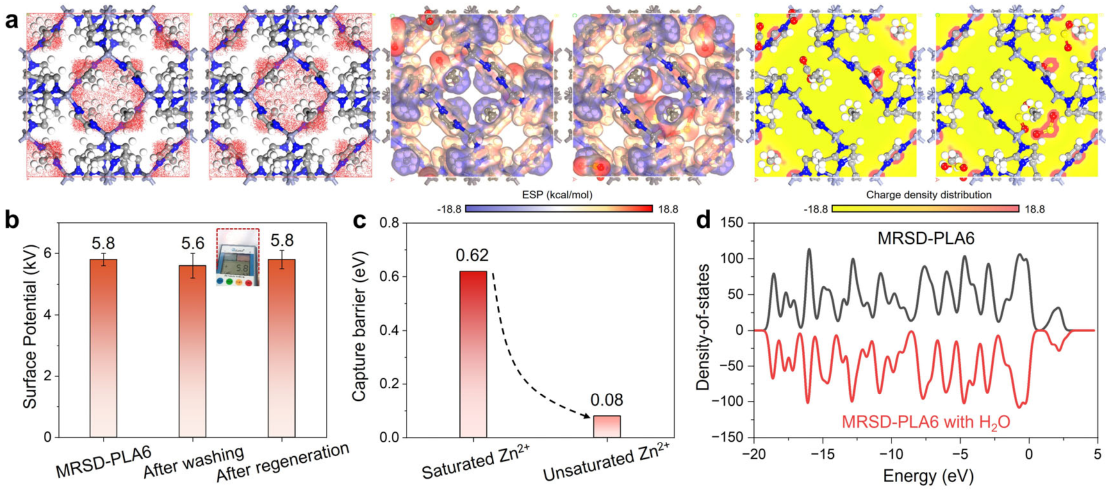

Figure S13. Verification of the charge capture-storage-regeneration cycle mechanism. a DFT calculations of MRSD-PLA6 and MRSD-PLA with H_2O. **b** Plots of surface potential after washing and regeneration. **c** Electron capture energy barrier of saturated Zn^{2+} and unsaturated Zn^{2+}. **d** Density of states for MRSD-PLA6 and MRSD-PLA with H_2O.

Analysis of the biodegradability and environmental friendliness of the PLA:

Many microorganisms, especially bacteria and fungi, can produce enzymes that hydrolyze PLA. Under suitable conditions, PLA can be broken down by microorganisms into water, carbon dioxide, and other substances.

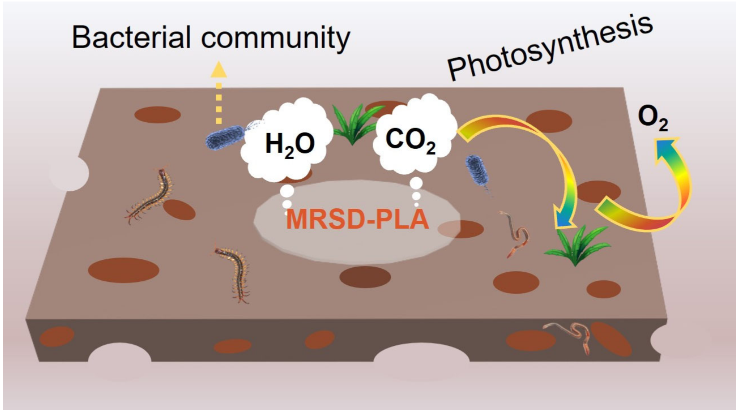

Figure S14. Schematic representation of the degradation of MRSD-PLA.

Microscopic morphological analysis of soil degradation processes:

SEM images reveal that the surfaces of P-PLA and MRSD-PLA6 fibers are colonized by a large number of microorganisms.

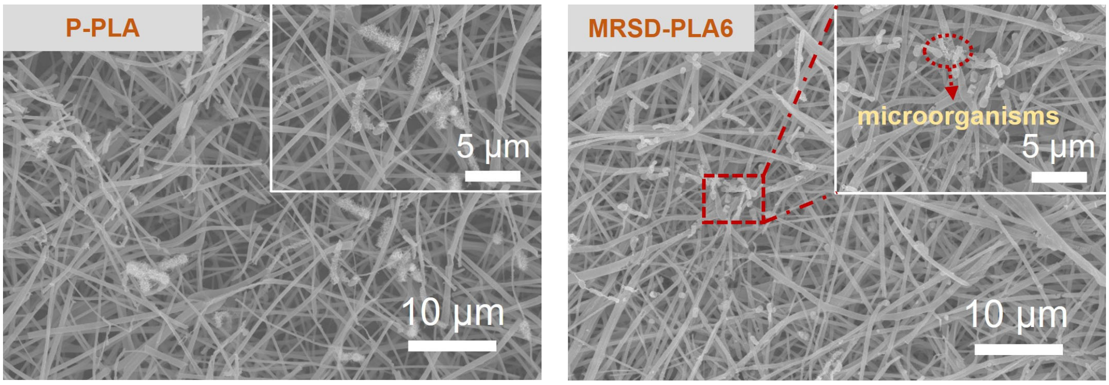

Figure S15. SEM images of P-PLA and MRSD-PLA6 after degradation.

Quantitative analysis of quality retention rate in the biodegradation process:

We have conducted additional soil burial degradation experiments under controlled conditions (40 °C, moist soil) based on the results shown in Figure 6e to systematically track the mass loss of both P-PLA and MRSD-PLA6 samples over a period of 84 days. The mass retention ratio (R_m) was calculated as:

$$R_m = \frac{m_t}{m_0} \times 100\% \tag{S7}$$

Where, R_m is the mass retention ratio, m_t is the mass at time *t*, m_0 is the initial mass.

The resulting mass retention plot (Figure S16) clearly demonstrates a gradual decrease in mass for both samples, with MRSD-PLA6 exhibiting a slightly slower initial degradation rate due to the presence of ZIF-8 and F-TiO_2, which temporarily impede microbial attachment and enzymatic hydrolysis. However, after 84 days, both membranes showed significant mass loss

(>75%), confirming their overall biodegradability. This quantitative data complements the existing visual and SEM-based morphological observations, providing a more comprehensive and objective evaluation of the degradation kinetics. Furthermore, the mass retention profile observed during the aqueous degradation process yielded results consistent with those previously obtained, further confirming the pronounced biodegradability and environmental compatibility of MRSD-PLA.

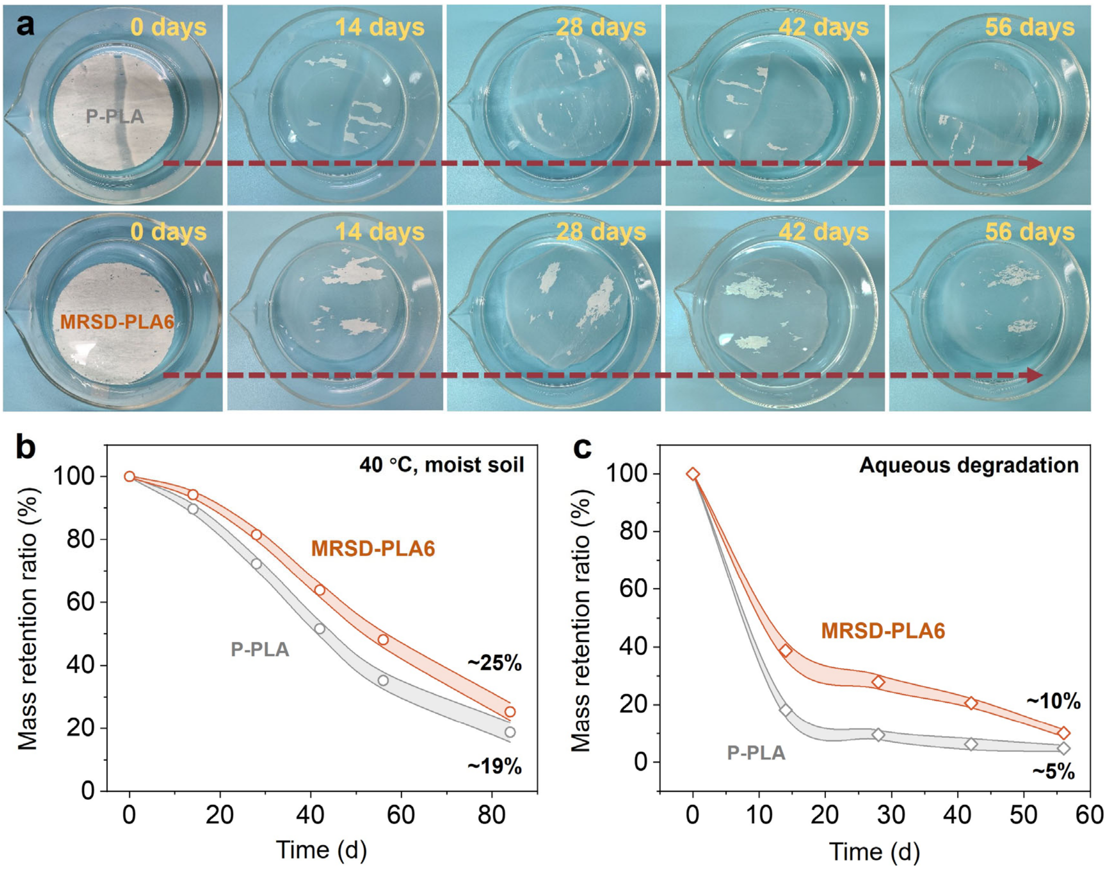

Figure S16. Biodegradation performance evaluation. **a** Hydrolysis process of P-PLA and MRSD-PLA6. **b** Mass retention rate diagram of P-PLA and MRSD-PLA6 membrane degradation in soil environment. **c** Mass retention rate diagram of P-PLA and MRSD-PLA6 membrane degradation in aquatic environment.

A comparison of filtration efficiency, pressure drop, and quality factor with commercial benchmark materials of comparable performance (e.g., melt-blown media for N95 or N99 masks, or fiberglass filters) under the same test conditions:

Filtration efficiency: MRSD-PLA6 achieved a PM$_{0.3}$ filtration efficiency of 99.3% at a flow rate of 10 L·min^{-1}, which is comparable to or exceeds that of commercial N99-grade melt-blown media (typically >99%) and fiberglass filters. Under high flow conditions (85 L·min^{-1}), MRSD-PLA6 maintained a filtration efficiency of 98.1%, significantly outperforming conventional melt-blown media, which often experience efficiency decay due to charge dissipation and structural compaction.

Pressure drop: The pressure drop across MRSD-PLA6 was only 51.9 Pa at 10 L·min^{-1}, which is substantially lower than that of melt-blown media (~100–150 Pa) and fiberglass filters (>200 Pa) under similar conditions. This indicates lower breathing resistance and energy consumption during operation.

Quality factor (*QF*): The *QF* value of MRSD-PLA6 reached 0.031 Pa^{-1}, which is higher than that of typical N95 melt-blown media (0.015–0.025 Pa^{-1}) and fiberglass filters (0.010–0.020 Pa^{-1}), demonstrating a superior balance between filtration performance and airflow resistance.

Table S1. Comparison of filtration performance between MRSD-PLA6 and commercial benchmark materials

Material	Flow rate (L·min^{-1})	PM$_{0.3}$ filtration efficiency (%)	Pressure drop (Pa)	Quality factor (Pa^{-1})
MRSD-PLA6	10	99.3	51.9	0.031
	85	98.1	215.0	0.018
N95 melt-blown media[11]	85	>95 N95 standard	~150-300	0.015-0.025
N99 melt-blown media[12]	85	>95 N99 standard	~200-350	0.012-0.020
Fiberglass filter[13]	85	>99.97	>250	0.010-0.020

Table S2. Evaluation of filtration efficiency at various face velocities

Airflow rate (L·min^{-1})	**Face velocity (cm·s^{-1})**	**Face velocity (m·s^{-1})**
10	2.2	0.022
32	6.9	0.069
65	14.1	0.141
85	18.0	0.180

References

1. Manchi, P. et al. PDA-Ag/TiO_2 nanoparticles-loaded electrospun nylon composite nanofibrous film-based triboelectric nanogenerators for wearable biomechanical energy harvesting and multifunctional sensors. *Adv. Funct. Mater.* **35**, 2416018 (2024).
2. Shi, S. et al. A bionic skin for health management: excellent breathability, in situ sensing, and big data analysis. *Adv. Mater.* **36**, 2306435 (2023).
3. Wang, X. et al. Biomimetic fibrous murray membranes with ultrafast water transport and evaporation for smart moisture-wicking fabrics. *ACS Nano* **13**, 1060-1070 (2018).
4. Yang, Y. et al. Ultrathin, ultralight dual-scale fibrous networks with high-infrared transmittance for high-performance, comfortable and sustainable $PM_{0.3}$ filter. *Nat. Commun.* **15**, 1586 (2024).
5. Wang, L. et al. Robust dual equivariant gradient antibacterial wound dressing-loaded artificial skin with nano-chitin particles via an electrospinning-reactive strategy. *Adv. Fiber Mater.* **7**, 204-218 (2024).
6. Han, Y., Ruan, K. & Gu, J. Multifunctional thermally conductive composite films based on fungal tree-like heterostructured silver nanowires@boron nitride nanosheets and aramid nanofibers. *Angew. Chem. Int. Ed.* **62**, e202216093 (2022).
7. Sun, Z. et al. ZIF-67/ZIF-8 and its derivatives for lithium sulfur batteries. *Adv. Funct. Mater.* **35**, 2414671 (2024).
8. Li, C.-B. et al. Deformation resistant monolithic hierarchical textures inducing stretchable superamphiphobicity with environmental adaptability and flame retardancy. *Nat. Commun.* **16**, 2729 (2025).
9. Xiao, L. et al. Fishnet-inspired 3D scaffold fabricated from mesh-like electrospun membranes promoted osteoporotic bone regeneration. *Adv. Fiber Mater.* **7**, 72-92 (2024).
10. Song, Y. et al. Co-CoSe heterogeneous fibers with strong interfacial built-in electric field as bifunctional electrocatalyst for high-performance Zn-air battery. *J. Colloid Interface Sci.* **677**, 140-150 (2025).

11 Leung, W. W.-F. & Sun, Q. Charged PVDF multilayer nanofiber filter in filtering simulated airborne novel coronavirus (COVID-19) using ambient nano-aerosols. *Sep. Purif. Technol.* **245**, 116887 (2020).

12 Zhang, S. et al. Spider-web-inspired $PM_{0.3}$ filters based on self-sustained electrostatic nanostructured networks. *Adv. Mater.* **32**, 2002361 (2020).

13 Wei, Z. et al. High-performance filter membrane composed of oxidized Poly (arylene sulfide sulfone) nanofibers for the high-efficiency air filtration. *J. Hazard. Mater.* **417**, 126033 (2021).